Two-scale computational approach using strain gradient theory at microlevel

Tomislav Lesičar, Zdenko Tonković, Jurica Sorić*

Faculty of Mechanical Engineering and Naval Architecture, University of Zagreb, Ivana Lučića 5, 10000 Zagreb, Croatia

ABSTRACT

Realistic description of heterogeneous material behavior demands more accurate modeling at macroscopic and microscopic scales. In this frame, the multiscale techniques employing homogenization scheme offer several solutions. Most recently developed two-scale scheme employing second-order homogenization requires the nonlocal theory at the macrolevel, while the classical local continuum theory is kept at the microlevel. In this paper, a new second-order computational homogenization scheme is proposed employing the higher-order theory at both macro- and microlevel. Discretization is performed by means of the C^1 finite element developed using the strain gradient theory. The new gradient boundary conditions employed on representative volume element (RVE) are derived. The relation between the internal length scale parameter and the RVE size has been found. The new procedure is tested on a benchmark example, where the results have been compared to the solutions obtained by the usual second-order homogenization using the local concept on the RVE.

1. Introduction

It is known that all engineering materials can be treated as heterogeneous at some scale of observation. Therein, material heterogeneity and anisotropy play a major role, because almost all materials are heterogeneous and anisotropic due to their natural structure, particularly on the microscopic scale. Profound demands on structural integrity in recent years lead to development and the application of new materials with complex microstructure giving desired material properties. Numerical analysis of mechanical behavior of this new class of materials emerges necessity for an advanced numerical tools employing more realistic material description. Heterogeneous metals such as nodular cast iron are widely used as the material of structural components in mechanical engineering. The ductile nodular cast iron consists of graphite nodules in a ferritic matrix providing large fatigue strength. The geometrical and material properties of the constituents making up the microstructure have a significant impact on the material behavior observed at the macroscale [1]. In addition, the external loading applied at the macroscale might cause changes in the microstructural morphology e.g., void formation, damage as well as cracking, which can put structural integrity at risk. Therefore, in order to assess structural integrity and to predict structural lifetime, an analysis of the evolving microstructure is necessary.

During recent years, a special attention has been directed to the investigation of the relations between the macroscopic material behavior and its microstructure. The determination of an effective material parameters was possible only by experiments or by semi-analytical homogenization methods based on the assumptions of constitutive behavior. Unfortunately, this class of methods cannot adequately capture physical mechanisms managing behavior of the microconstituents. In a multiscale approach, the response of coarse scale problem incorporates physical understanding of material behavior at the lower scales. Firstly, the homogenization concept has been developed in the framework of a classical local continuum theory. In this concept several homogenization approaches are available, such as the mathematical method of homogenization, the Mori-Tanaka method, the double inclusion model, the numerical homogenization, asymptotic homogenization etc., as can be found in [2–4]. However, in more recent formulations several computational homogenization approaches have been used [5–12]. These computational procedures are based on the solution of two boundary value problems, one at the macroscopic and one at the microscopic scale. The results obtained by the simulation of a microscopic representative sample of material named Representative Volume Element (RVE) are used at the macrolevel analysis. Thus, the computational multiscale approach does not require an explicit constitutive relation at the macrolevel, which allows modeling of complex microstructure geometry as well as deformation responses. When in the scale transition procedure only the first displacement gradient is involved, whereby the stress at a material point depends only on the strain (and other state variables) at the same point, this method is referred as the first-order homogenization [13–15]. However, the first-order computational homogenization relies on the intrinsic assumption

of uniformity of the macroscopic stress and strain fields appointed to a representative volume element (RVE). Due to uniformity assumption, the first-order homogenization is not adequate for the problems dealing with high gradients, where the macroscopic fields can vary rapidly. Therefore, only simple loading cases can be studied, which is considered as a deficiency. Another major shortcoming of the first-order homogenization approach is an inability to encompass microstructural size effects in a material, such as strain localization phenomena and material softening.

The mentioned shortcomings of the first-order approach have been overwhelmed in an extended formulation proposed in a second-order computational homogenization procedure [8,16,17]. This computational strategy comprises a nonlocal continuum theory at the macroscale, which takes into account the influence of a surrounding material on the behavior of a considered material point [18,19]. Herein, the size effects can be accounted for through the RVE size. The microstructural level represented by the RVE is treated as an ordinary local continuum, see [20,21], which is in this case able to capture more complex deformation modes. For the numerical implementation of the multiscale framework, finite element method is the most popular approach. To solve boundary value problems employing the nonlocal theory which is in second-order homogenization adopted at the macrolevel, C^1 continuous interpolations should by applied in appropriate finite element formulations, where displacements, as well as displacement gradients (strains) should be continuous functions. On the other hand, at the microstructural level classical theory is preserved, where the standard finite elements employing C^0 continuity are usually used for discretization. Thus, based on the aforementioned numerical implementation aspects, the multiscale scheme employing the second-order computational homogenization, which comprises the nonlocal theory at the macrolevel and the local theory on the microlevel in the following text will be referred as the NL-SL (nonlocal-standard local) second-order homogenization. Unfortunately, the NL-SL second-order computational homogenization approach suffers from difficulties in the scale transition methodology due to the coupling between the nonlocal theory at the macroscale and the local concept on the RVE. Namely, the second-order macrolevel gradient cannot be related to the micro-level higher-order gradient as a true volume average. Therefore, in the micro-to-macro scale transition, after resolving Hill-Mandel energy condition, the homogenized double stress requires a modified definition at the microstructural level. Furthermore, in case of generalized periodic boundary conditions, an artificial stress concentration appears at the RVE corner nodes, as result of suppressed microfluctuations at the RVE corners [17]. In order to cope with this problem, some regularization methods have been proposed. A substantially different approach has been derived in [21,22] for the multiscale kinematics, where zero projection of the microfluctuations at the macrolevel is enforced through the principle of orthogonality. The orthogonality is enforced by a vanishing surface integral of the micro-macro variable scalar product. Even though such formulation has notable advantages, again, some relaxed constraints on the fluctuation field are required to avoid stress concentrations at the corners. Similar solution has been recently proposed in [23], using the method of multiscale virtual power. In this approach, the external body forces and macroscale displacements are used in the macro-to-micro scale transition. A novel concept of conservation of kinematical quantities is introduced and used for derivation of the boundary conditions and homogenized quantities. This approach can be considered as an extension of the framework derived in [17,22], since the resulting relations in the absence of the volume forces and inertia effects coincide with the relations derived in the above mentioned references. Even though significant research has been published on the macro-to-micro scale transition in the second-order homogenization framework, this challenging problem still remains open for further studies.

In addition, the discretization of the macrostructural level in the NL-SL scheme is usually performed using mixed finite element formula-

tions, where the C^1 continuity requirements are fulfilled in a weak sense, via Lagrange multiplier or penalty method [24–29]. But, the mixed finite element formulations show a poor behavior compared to the C^1 finite elements [29–31]. Besides the mixed finite element formulation, other approaches can be used for solving gradient problems, such as the discontinuous Galerkin method [32,33], the meshless methods [34–36], or the boundary element methods [37–39]. A comprehensive overview can be found in [40]. Despite large efforts, an efficient numerical formulation for solving strain gradient problems is still unresolved.

In this paper the authors propose a new second-order computational homogenization scheme employing the nonlocal theory at both scales. Therein, the mathematical consistency of the transition methodology is ensured, considering conforming continuum theories used at different scales. The computational scheme is derived adopting the gradient elasticity theory and small strain setting. The discretization at both the macro and microlevel is performed by the C^1 continuity plane strain triangular finite element derived and verified earlier in [41,42]. In that sense, the newly proposed framework derived in this contribution will be referenced as the NL-NL (nonlocal-nonlocal) second-order computational homogenization. The macro-to-micro scale transition methodology is derived using the gradient displacement and gradient generalized periodic boundary conditions. A consistent NL-NL homogenization scheme has been proposed. The derived scale transition methodology, as well as homogenization procedure were embedded into the finite element program ABAQUS by means of FORTRAN subroutines. The performance and accuracy of the proposed approach has been verified on an elastic shear layer example.

The paper is organized as follows. In Section 2 the gradient theory is discussed and the constitutive relations of the Aifantis gradient elasticity theory are displayed. Section 3 deals with the numerical implementation of the Aifantis theory into finite element method. The basic relations of the C^1 triangular finite element are derived. Also, the physical role of the element nodal degrees of freedom is discussed. Some issues of implementation of a non-standard finite element into the commercial FE software ABAQUS are described. In Section 4, a new gradient-enhanced second-order computational homogenization is developed, where the complete micro-macro transition procedure is explained. The dependence of the RVE size on the length scale parameter of the Aifantis gradient theory is investigated. The performance of the newly developed homogenization procedure is verified in Section 5. The standard benchmark problem of shear layer is discussed, where the accuracy of the results obtained by the NL-NL algorithm is confirmed by the comparison to the NL-SL homogenization scheme available in the literature.

2. Higher-order continuum theory

2.1. Small strain second-gradient continuum formulation

In a classical small strain continuum theory, kinematical behavior at time t is described by the vector of the displacement field $\mathbf{u} = u_i\mathbf{e}_i$. The displacement gradient describes the second-order strain tensor expressed by the components as

$$\varepsilon_{ij} = \frac{1}{2}(u_{i,j} + u_{j,i}). \tag{1}$$

In the second-gradient continuum theory, a third-order strain gradient tensor $^3\boldsymbol{\eta}$ is introduced, which is defined as gradient of the strain tensor

$$^3\boldsymbol{\eta} = \eta_{ijk}\mathbf{e}_i \otimes \mathbf{e}_j \otimes \mathbf{e}_k = \nabla \otimes \boldsymbol{\varepsilon}, \tag{2}$$

with a minor symmetry in the last two indices $\eta_{ijk} = \eta_{ikj}$, [43]. Accordingly, the variation of the strain energy density function may be expressed in terms of both the strain and the strain gradient as

$$\delta W = \frac{\partial W}{\partial \boldsymbol{\varepsilon}} : \delta \boldsymbol{\varepsilon} + \frac{\partial W}{\partial^3 \boldsymbol{\eta}} : \delta^3 \boldsymbol{\eta} = \boldsymbol{\sigma} : \delta \boldsymbol{\varepsilon} + {}^3 \boldsymbol{\mu} : \delta^3 \boldsymbol{\eta}. \tag{3}$$

In Eq. (3), $\boldsymbol{\sigma} = \sigma_{ij} \mathbf{e}_i \otimes \mathbf{e}_j$ is the Cauchy stress tensor, and ${}^3 \boldsymbol{\mu} = \mu_{kji} \mathbf{e}_k \otimes \mathbf{e}_j \otimes \mathbf{e}_i$ represents the third-order double stress tensor, symmetric in the first two indices. After some mathematical rearrangements, relation (3) may be rewritten in the following form

$$\delta W = \nabla \cdot (\boldsymbol{\sigma} \cdot \delta \mathbf{u}) - (\nabla \cdot \boldsymbol{\sigma}) \cdot \delta \mathbf{u} + \nabla \cdot [{}^3 \boldsymbol{\mu} : (\nabla \otimes (\delta \mathbf{u}))] - \nabla \cdot (\delta \mathbf{u} \cdot (\nabla \cdot {}^3 \boldsymbol{\mu})) + (\nabla \cdot (\nabla \cdot {}^3 \boldsymbol{\mu})) \cdot \delta \mathbf{u}. \tag{4}$$

Furthermore, integrating Eq. (4) over the volume and applying divergence theorem results in the internal work variation

$$\delta W^{\text{int}} = \int_A [\mathbf{n} \cdot (\boldsymbol{\sigma} - (\nabla \cdot {}^3 \boldsymbol{\mu})) \cdot \delta \mathbf{u}] dA - \int_V \{[\nabla \cdot (\boldsymbol{\sigma} - (\nabla \cdot {}^3 \boldsymbol{\mu}))] \cdot \delta \mathbf{u}\} dV + \int_A [(\mathbf{n} \cdot {}^3 \boldsymbol{\mu}) : (\nabla \otimes (\delta \mathbf{u}))] dA, \tag{5}$$

with $\mathbf{n}$ as a unit outward normal vector to the body surface A. Therein, the gradient of displacement variation $\nabla \otimes (\delta \mathbf{u})$ is decomposed into surface and normal gradient as

$$\nabla \otimes (\delta \mathbf{u}) = \nabla^A \otimes (\delta \mathbf{u}) + \mathbf{n} \otimes D \otimes (\delta \mathbf{u}), \tag{6}$$

where the surface gradient is defined as

$$\nabla^A = \nabla \cdot (\mathbf{I} - \mathbf{n} \otimes \mathbf{n}), \tag{7}$$

and D is the normal gradient operator

$$D = \mathbf{n} \cdot \nabla. \tag{8}$$

In Eq. (7), $\mathbf{I}$ represents a second-order unit tensor. Applying the aforementioned decomposition on the last subintegral term in relation (5), after some straightforward mathematical manipulations, the variation of internal work can be rearranged as

$$\delta W^{\text{int}} = \int_A [\mathbf{n} \cdot (\boldsymbol{\sigma} - (\nabla \cdot {}^3 \boldsymbol{\mu})) \cdot \delta \mathbf{u}] \, dA + \int_A [(\nabla^A \cdot \mathbf{n}) \otimes \mathbf{n} \cdot (\mathbf{n} \cdot {}^3 \boldsymbol{\mu}) \cdot \delta \mathbf{u}] \, dA - \int_A [\nabla^A \cdot (\mathbf{n} \cdot {}^3 \boldsymbol{\mu}) \cdot \delta \mathbf{u}] \, dA - \int_V [\nabla \cdot (\boldsymbol{\sigma} - (\nabla \cdot {}^3 \boldsymbol{\mu})) \cdot \delta \mathbf{u}] \, dV + \int_A [(\mathbf{n} \cdot {}^3 \boldsymbol{\mu} \cdot \mathbf{n}) \cdot (D \otimes (\delta \mathbf{u}))] dA. \tag{9}$$

As usual, the variation of external work is expressed as

$$\delta W^{\text{ext}} = \int_A (\mathbf{t} \cdot \delta \mathbf{u}) \, dA + \int_A [\boldsymbol{\tau} \cdot (D \otimes (\delta \mathbf{u}))] \, dA, \tag{10}$$

where $\mathbf{t}$ is the surface traction. As evident, according to the nonlocal theory discussed here, the external work is extended by the higher order term of double surface traction $\boldsymbol{\tau}$. For simplicity, the body forces are here neglected. As well known, the traction boundary conditions and equilibrium equation may be extracted from the principle of virtual work. Thus, the boundary conditions acting on part of the surface A, according to (10) are

$$\mathbf{t} = \mathbf{n} \cdot (\boldsymbol{\sigma} - (\nabla \cdot {}^3 \boldsymbol{\mu})) + (\nabla^A \cdot \mathbf{n}) \otimes \mathbf{n} \cdot (\mathbf{n} \cdot {}^3 \boldsymbol{\mu}) - \nabla^A \cdot (\mathbf{n} \cdot {}^3 \boldsymbol{\mu}) \tag{11}$$

and

$$\boldsymbol{\tau} = \mathbf{n} \cdot {}^3 \boldsymbol{\mu} \cdot \mathbf{n}. \tag{12}$$

Finally, the equilibrium equation may be written in the following form

$$\nabla \cdot [\boldsymbol{\sigma} - (\nabla \cdot {}^3 \boldsymbol{\mu})] = \mathbf{0}. \tag{13}$$

2.1.1. Aifantis gradient elasticity theory

In a higher-order continuum theory developed by [43], various forms of strain energy function relying on different grouping of strain gradient terms are introduced. In the Mindlin's form II, the second-order terms are expressed as the strain gradient tensor. It is important to mention that the form II is the Mindlin's form with the symmetric stress tensor. The modified case of the Mindlin's form II has been proposed by Aifantis in [44], where most of the gradient coefficients are neglected. Accordingly, the strain energy density is defined as

$$W = \frac{1}{2} \lambda \varepsilon_{ii} \varepsilon_{jj} + \mu \varepsilon_{ij} \varepsilon_{ij} + l^2 \left(\frac{1}{2} \lambda \varepsilon_{ii,k} \varepsilon_{jj,k} + \mu \varepsilon_{ij,k} \varepsilon_{ij,k} \right). \tag{14}$$

In Eq. (14), λ and μ are Lamé constants, while l^2 represents microstructural parameter (material length scale). According to the strain energy function (14), the stress and the second-order stress may be expressed as

$$\boldsymbol{\sigma} = \frac{\partial W}{\partial \varepsilon_{ij}} = (\lambda \, \text{tr} \, \boldsymbol{\varepsilon}) \otimes \mathbf{I} + 2\mu \, \boldsymbol{\varepsilon}, \tag{15}$$

$${}^3 \boldsymbol{\mu} = \frac{\partial W}{\partial \eta_{kji}} = l^2 [(\lambda \, \text{tr}(\nabla \otimes \boldsymbol{\varepsilon})) \otimes \mathbf{I} + 2\mu (\nabla \otimes \boldsymbol{\varepsilon})]. \tag{16}$$

3. Finite element implementation

3.1. Finite element derivation

The Aifantis strain gradient theory has been embedded into finite element framework by means of the three node triangular finite element named C1PE3, derived by the authors of this contribution in [41,45]. For the sake of completeness, only a short overview of the element derivation will be presented here. The element is shown in Fig. 1. It contains twelve degrees of freedom (DOF) per node, and it satisfies C^1 continuity with assumptions of the plane strains. The element displacement field is approximated by a fifth order polynomial.

The element displacement field is approximated by the usual matrix relation

$$\mathbf{u} = \mathbf{N} \mathbf{v}, \tag{17}$$

where $\mathbf{N}$ is the shape function matrix and $\mathbf{v}$ is the nodal degrees of freedom vector. The strain field $\boldsymbol{\varepsilon}$ is approximated by first derivatives of the shape functions compiled in the $\mathbf{B}$ matrix, while the higher-order gradients are expressed as

$$\boldsymbol{\varepsilon}_{x_1} = \begin{pmatrix} \varepsilon_{11,1} \\ \varepsilon_{22,1} \\ 2\varepsilon_{12,1} \end{pmatrix} = \begin{pmatrix} u_{1,11} \\ u_{2,21} \\ u_{1,21} + u_{2,11} \end{pmatrix} = \mathbf{B}_{\eta_1} \mathbf{v}, \tag{18}$$

$$\boldsymbol{\varepsilon}_{x_2} = \begin{pmatrix} \varepsilon_{11,2} \\ \varepsilon_{22,2} \\ 2\varepsilon_{12,2} \end{pmatrix} = \begin{pmatrix} u_{1,12} \\ u_{2,22} \\ u_{1,22} + u_{2,12} \end{pmatrix} = \mathbf{B}_{\eta_2} \mathbf{v}. \tag{19}$$

Herein the matrices $\mathbf{B}_{\eta_1}$ and $\mathbf{B}_{\eta_2}$ contain the gradients of the strain matrix $\mathbf{B}$ with respect to the coordinates x_1 and x_2, respectively. The Cauchy stress tensor is computed using the usual constitutive relation

$$\boldsymbol{\sigma} = \mathbf{C} \mathbf{B} \mathbf{v}. \tag{20}$$

The double stress tensors are introduced as energy conjugates to $\boldsymbol{\varepsilon}_{x_1}$ and $\boldsymbol{\varepsilon}_{x_2}$, according to (16) as

$$\boldsymbol{\mu}_{x_1} = \begin{pmatrix} \mu_{111} \\ \mu_{122} \\ \mu_{112} \end{pmatrix} = l^2 \mathbf{C} \mathbf{B}_{\eta_1} \mathbf{v}, \tag{21}$$
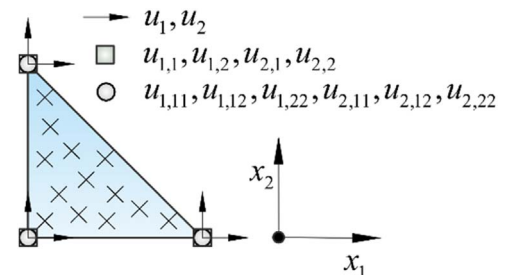

Fig. 1. C^1 triangular finite element.

$$\boldsymbol{\mu}_{x_2} = \begin{pmatrix} \mu_{211} \\ \mu_{222} \\ \mu_{212} \end{pmatrix} = l^2 \mathbf{CB}_{\eta_2} \mathbf{v}. \tag{22}$$

As evident, the double stresses in the Aifantis theory are related to the strain gradients via the elasticity matrix $\mathbf{C}$ also appearing in (20). As a measure of nonlocality, the microstructural parameter l^2 is also included in the constitutive relations (21) and (22). This significantly simplifies the problems regarding experimental determination of a higher-order constitutive model, since the classical stress-strain experimental data remain unchanged. After usual finite element mathematical manipulations [41], the finite element equation $\mathbf{Kv} = \mathbf{F}$ is derived, where the stiffness matrix may be expressed as

$$\mathbf{K} = \mathbf{K}_l + l^2(\mathbf{K}_{x_1} + \mathbf{K}_{x_2}), \tag{23}$$

consisting of the submatrices

$$\mathbf{K}_l = \int_A (\mathbf{B}^T \mathbf{CB}) \, dA, \tag{24}$$

$$\mathbf{K}_{x_1} = \int_A \left(\mathbf{B}_{\eta_1}^T \mathbf{CB}_{\eta_1} \right) dA, \tag{25}$$

$$\mathbf{K}_{x_2} = \int_A \left(\mathbf{B}_{\eta_2}^T \mathbf{CB}_{\eta_2} \right) dA. \tag{26}$$

The nodal force vector takes the usual form consisting of the surface traction $\mathbf{t}$ and the double surface traction $\boldsymbol{\tau}$ integrated over the element edge s as shown in [41]

$$\mathbf{F} = \int_s (\mathbf{N}^T \mathbf{t} + (\nabla \otimes \mathbf{N})^T \boldsymbol{\tau} \mathbf{n}) \, ds, \tag{27}$$

where the vector $\mathbf{n}$ stands for the edge normal vector.

The element has been implemented into the FE program ABAQUS [46] using the user element subroutine UEL. For numerical integration of the stiffness matrices and force vector, the reduced Gauss integration technique with 13 integration points has been used, instead of the full integration scheme with 25 points. Their positions are given in Fig. 1. As presented in [41], the reduced integration technique provides quite satisfactory results and it is more convenient for the multiscale analysis, where a discretized RVE is assigned to each point. The element does not contain spurious zero energy modes and passes the patch test. In addition, the element satisfies standard benchmark tests [16,41].

3.2. Physical interpretation of nodal degrees of freedom

In the derived finite element formulation, the twelve DOF per node are available, where, next to displacements, first and second derivatives are also included. Availability of higher-order derivatives in the nodes gives to the element extreme flexibility for achievement of various deformation modes, even by a single element, which are not reachable for a classical C° elements without some additional constraints.

On the other hand, dealing with the derivatives represents a delicate and a demanding task. Boundary conditions regarding the derivative DOF are not specifically restricted only on an outer boundary of the numerical model. There might be necessity for constraining the derivative DOF through the whole numerical model in order to obtain a desired deformed shape as well as the strain and strain gradient distributions. Basically, if the derivative DOF are not appropriately handled, the consequences can be unpredictable. Assuming that the displacement degrees of freedom are easily resolved, the deformed shape should lead to some realistic behavior, but it is not guaranteed. Without right combination of the displacement derivative DOF on the boundaries and throughout the model, the distribution of the displacements as well as the displacement gradients through the model cannot be taken as reliable. In order to cope with these problems, clear physical interpretation of the nodal DOF is required.

The displacement components u_1 and u_2 are inherent from classical
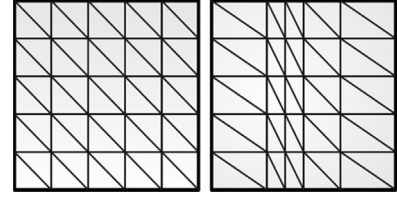

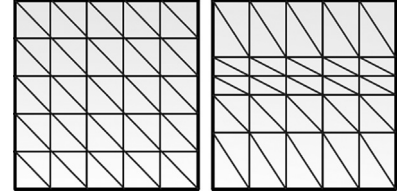**Fig. 2.** Physical interpretation of nodal degree of freedom $u_{1,11}$.

Fig. 3. Physical interpretation of nodal degree of freedom $u_{2,22}$.

finite elements and further discussion about them is unnecessary. The first derivatives $u_{1,1}$ and $u_{2,2}$ represent longitudinal or lateral strains and no significant difficulties managing them in the boundary condition setting should appear. In addition, the twist degrees of freedom $u_{1,2}$ and $u_{2,1}$ are generally known from the classical continuum theory, and their use in the boundary conditions can also be resolved without any issues. Dealing with the second derivatives, which usually do not come as nodal variables becomes more difficult. Hence, in the following, the physical meaning of each second derivative DOF will be visualized.

The nodal variables $u_{1,11}$ and $u_{2,22}$ are physically interpreted as the rates of the change of normal strains in x_1 and x_2 directions, respectively. As shown in Figs. 2 and 3, if we prescribe only these components on a square model, we can see the movement of an interior material in the loading directions.

Next, the nodal degrees of freedom $u_{1,22}$ and $u_{2,11}$ are solely prescribed on a square model represented in Figs. 4 and 5, respectively. It can be observed that they physically represent the in-plane curvatures.

Prescribing only the mixed second derivatives $u_{1,21}$ and $u_{2,12}$ on a square model gives the deformation responses presented in Figs. 6 and 7.

It is obvious that availability of all these DOF gives to the element high superiority to capture various deformation responses, even with a coarse mesh. However, to achieve meaningful results, they must be appropriately handled.

4. Strain-gradient second-order computational homogenization scheme

4.1. Macro-to-micro scale transition

In the following, the basic of the strain-gradient second-order computational homogenization procedure which preserves nonlocal theory on the RVE is explained. The geometry of the RVE is assumed to be square shaped, as usual, with the coordinate system placed in the centroid, as displayed in Fig. 8. All variables appearing at the microstructural level are denoted by the subscript "m", while the macrostructural quantities are referenced by the index "M". The RVE
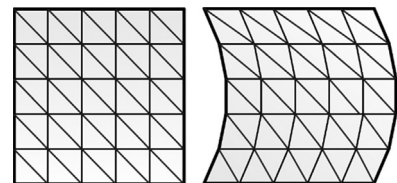

Fig. 4. Physical interpretation of nodal degree of freedom $u_{1,22}$.
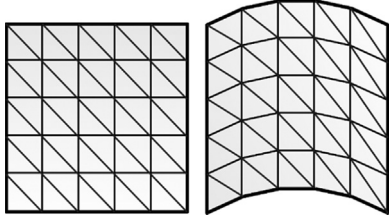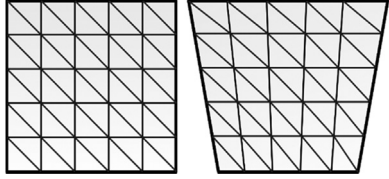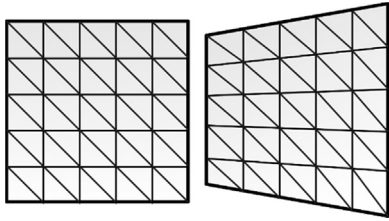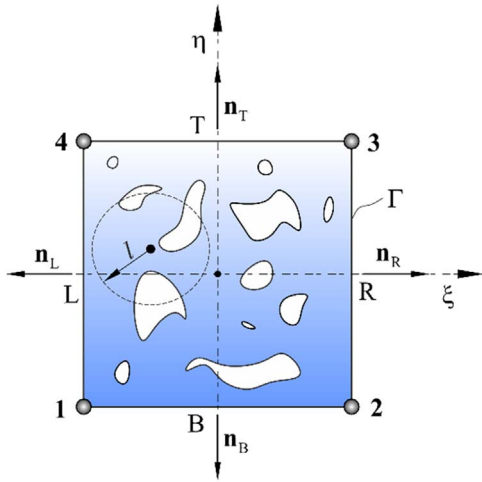
Fig. 5. Physical interpretation of nodal degree of freedom $u_{2,11}$.

Fig. 6. Physical interpretation of nodal degree of freedom $u_{1,21}$.

Fig. 7. Physical interpretation of nodal degree of freedom $u_{2,12}$.

Fig. 8. Representative volume element.

displacement field is represented by a Taylor series expansion depending on the macrolevel strain $\boldsymbol{\varepsilon}_M$ and strain gradient $\nabla \otimes \boldsymbol{\varepsilon}_M$, in accordance with Aifantis theory used. Based on the aforementioned, the displacement imposed along the RVE boundaries is defined as

$$\mathbf{u}_m = \boldsymbol{\varepsilon}_M \cdot \mathbf{x} + \frac{1}{2}(\mathbf{x} \cdot (\nabla \otimes \boldsymbol{\varepsilon}_M) \cdot \mathbf{x}) + \mathbf{r}. \tag{28}$$

Here $\mathbf{x}$ and $\mathbf{r}$ represent the microlevel spatial coordinate and the microfluctuation field, respectively. Based on the microlevel displacements (28), the microlevel strain tensor may be expressed in the form

$$\boldsymbol{\varepsilon}_m = \boldsymbol{\varepsilon}_M + (\nabla \otimes \boldsymbol{\varepsilon}_M) \cdot \mathbf{x} + \nabla_m \otimes \mathbf{r}. \tag{29}$$

Since the nonlocal theory is used on the RVE, the microscale strain gradients can be directly derived as

$$\nabla_m \otimes \boldsymbol{\varepsilon}_m = \nabla \otimes \boldsymbol{\varepsilon}_M + \nabla_m \otimes (\nabla_m \otimes \mathbf{r}). \tag{30}$$

Obviously, the derivation of Eq. (30) in the NL-NL scheme is much

more straightforward compared to the lengthy procedure required in the NL-SL homogenization [17,47,48]. As known, the volume average of the gradients at the microlevel must be equal to the conjugate quantity at the macrostructural material point. In order to satisfy this constraint in Eq. (29), it is obvious that

$$\frac{1}{V} \int_V (\nabla_m \otimes \mathbf{r}) dV = \frac{1}{V} \int_\Gamma (\mathbf{n} \otimes \mathbf{r}) d\Gamma = \mathbf{0}. \tag{31}$$

As demonstrated, the volume integral is transformed into a surface integral over the RVE boundary Γ by virtue of Gauss theorem. Accordingly, using Eq. (30), the following integral constraint rises

$$\frac{1}{V} \int_V (\nabla_m \otimes (\nabla_m \otimes \mathbf{r})) dV = \frac{1}{V} \int_\Gamma (\mathbf{n} \otimes (\nabla_m \otimes \mathbf{r})) d\Gamma = {}^3\mathbf{0}. \tag{32}$$

The constraints (31) and (32) should be satisfied through appropriate choice of boundary conditions. Clearly, the introduction of the second-order gradients on the microstructural scale significantly decreases mathematical complexity of the derivation procedure. This can be proved in comparison to the previous contributions, e. g. [17,47,48], where the local theory is adopted at the microscale (NL-SL homogenization). Since only local variables are defined on the RVE, the special assumptions on definition of higher-order gradients have to be imposed, which raises the complexity of the scale transition procedure.

In the NL-NL homogenization procedure proposed here, the gradient displacement boundary conditions (b. c.) and the gradient generalized periodic b. c. are imposed along the RVE boundaries. Essentially, those boundary conditions have already been used in the NL-SL homogenization, but they are extended on the displacement gradients as nodal variables in the NL-NL homogenization. The RVE displacement (28) of the ith node on the RVE boundary can be rewritten into the matrix form as

$$\mathbf{u}_i = \mathbf{D}_i^T \boldsymbol{\varepsilon}_M + (\mathbf{H}_1^T)_i (\boldsymbol{\varepsilon}_{x_1})_M + (\mathbf{H}_2^T)_i (\boldsymbol{\varepsilon}_{x_2})_M + \mathbf{r}_i. \quad i = 1 \dots m \tag{33}$$

Herein the coordinate matrices $\mathbf{D}$, $\mathbf{H}_1$ and $\mathbf{H}_2$ are introduced, and m is the number of nodes on the RVE boundaries. More details on the coordinate matrices and their derivations can be found in [49]. $(\boldsymbol{\varepsilon}_{x_1})_M$ and $(\boldsymbol{\varepsilon}_{x_2})_M$ are the macrolevel strain gradients with respect to x_1 and x_2, respectively, defined according to Eqs. (18) and (19). The rigid body movements should be suppressed [16], where caution has to be taken on the physical interpretation of the nodal DOF. In case of gradient displacement b. c. all boundary nodes are prescribed, and the microfluctuations have to be suppressed. For the gradient generalized periodic b. c., only corner nodes should be prescribed together with the neglecting of the microfluctuation field. The remaining boundary nodes are kinematically related based on the periodicity assumption ($\mathbf{r}_R = \mathbf{r}_L$, $\mathbf{r}_T = \mathbf{r}_B$), see Fig. 8. Using the periodicity according to relation (33) leads to the equations

$$\mathbf{u}_R - \mathbf{u}_L = (\mathbf{D}_R^T - \mathbf{D}_L^T)\boldsymbol{\varepsilon}_M + ((\mathbf{H}_1^T)_R - (\mathbf{H}_1^T)_L)(\boldsymbol{\varepsilon}_{x_1})_M$$
$$+ ((\mathbf{H}_2^T)_R - (\mathbf{H}_2^T)_L)(\boldsymbol{\varepsilon}_{x_2})_M, \tag{34}$$

$$\mathbf{u}_T - \mathbf{u}_B = (\mathbf{D}_T^T - \mathbf{D}_B^T)\boldsymbol{\varepsilon}_M + ((\mathbf{H}_1^T)_T - (\mathbf{H}_1^T)_B)(\boldsymbol{\varepsilon}_{x_1})_M$$
$$+ ((\mathbf{H}_2^T)_T - (\mathbf{H}_2^T)_B)(\boldsymbol{\varepsilon}_{x_2})_M. \tag{35}$$

As may be observed, the periodicity Eqs. (34) and (35) prescribe constraints not only on the displacements, but also on the first and second displacement derivatives available as the nodal DOF. This gives possibility to prescribe the complete second-order gradient field from the macrolevel on the RVE boundaries without need for the microfluctuation integrals, which is not the case in the NL-SL homogenization.

4.2. Micro-to-macro scale transition

In the homogenization of the macrostructural variables, the math-

ematical consistency of the NL-NL approach is again expected due to the fact that the second-order gradients are introduced at the microstructural level. In this context, the variation of the work performed has the same definition on both scales, which is experienced also in the first-order homogenization [13]. Thus, in the NL-NL homogenization the Hill-Mandel energy condition is defined as

$$\frac{1}{V}\int_V (\boldsymbol{\sigma}_m : \delta\boldsymbol{\varepsilon}_m + {}^3\boldsymbol{\mu}_m : (\nabla_m \otimes \delta\boldsymbol{\varepsilon}_m))\,dV = \boldsymbol{\sigma}_M : \delta\boldsymbol{\varepsilon}_M + {}^3\boldsymbol{\mu}_M : (\nabla \otimes \delta\boldsymbol{\varepsilon}_M).$$

(36)

For comparison, in the NL-SL homogenization, the left-hand side of Eq. (36) consists only of the term $\frac{1}{V}\int_V (\boldsymbol{\sigma}_m : \delta\boldsymbol{\varepsilon}_m)\,dV$, which consequently yields the averaging of the higher-order stress only by the Cauchy stress, as presented in [17,47]. Substitution of (29) and (30) into (36) leads to

$$\left(\frac{1}{V}\int_V \boldsymbol{\sigma}_m\,dV\right) : \delta\boldsymbol{\varepsilon}_M + \frac{1}{V}\int_V (\boldsymbol{\sigma}_m : (\nabla_m \otimes \delta\mathbf{r}))dV$$
$$+ \left(\frac{1}{V}\int_V ({}^3\boldsymbol{\mu}_m + \boldsymbol{\sigma}_m \otimes \mathbf{x})\,dV\right) : (\nabla \otimes \delta\boldsymbol{\varepsilon}_M)$$
$$+ \frac{1}{V}\int_V [{}^3\boldsymbol{\mu}_m : (\nabla_m \otimes (\nabla_m \otimes \delta\mathbf{r}))]\,dV = \boldsymbol{\sigma}_M : \delta\boldsymbol{\varepsilon}_M + {}^3\boldsymbol{\mu}_M : (\nabla \otimes \delta\boldsymbol{\varepsilon}_M).$$

(37)

To achieve the Hill-Mandel condition (36), it is obvious that the integral terms containing microfluctuations in Eq. (37) should vanish. Accordingly, the following relation holds

$$\frac{1}{V}\int_V [\boldsymbol{\sigma}_m : (\nabla_m \otimes \delta\mathbf{r}) + {}^3\boldsymbol{\mu}_m : (\nabla_m \otimes (\nabla_m \otimes \delta\mathbf{r}))]\,dV = 0.$$

(38)

The second term on the left hand side of Eq. (38) can be rearranged as

$$\frac{1}{V}\int_V [{}^3\boldsymbol{\mu}_m : (\nabla_m \otimes (\nabla_m \otimes \delta\mathbf{r}))]\,dV = \frac{1}{V}\int_V [\nabla_m \cdot ({}^3\boldsymbol{\mu}_m : (\nabla_m \otimes \delta\mathbf{r}))]\,dV$$
$$- \frac{1}{V}\int_V [(\nabla_m \cdot {}^3\boldsymbol{\mu}_m) : (\nabla_m \otimes \delta\mathbf{r})]\,dV$$

(39)

Thereafter, inserting of Eq. (39) into (38), gives

$$\frac{1}{V}\int_V [(\boldsymbol{\sigma}_m - \nabla_m \cdot {}^3\boldsymbol{\mu}_m) : (\nabla_m \otimes \delta\mathbf{r})]\,dV + \frac{1}{V}\int_V [\nabla_m \cdot ({}^3\boldsymbol{\mu}_m : (\nabla_m \otimes \delta\mathbf{r}))]\,dV$$
$$= 0.$$

(40)

Here the first term on the left hand side of (40) can be rewritten to

$$\frac{1}{V}\int_V [(\boldsymbol{\sigma}_m - \nabla_m \cdot {}^3\boldsymbol{\mu}_m) : (\nabla_m \otimes \delta\mathbf{r})]\,dV = \frac{1}{V}\int_V \{\nabla_m \cdot [(\boldsymbol{\sigma}_m - \nabla_m \cdot {}^3\boldsymbol{\mu}_m) \cdot \delta\mathbf{r}]\}\,dV$$
$$- \frac{1}{V}\int_V \{[\nabla_m \cdot (\boldsymbol{\sigma}_m - \nabla_m \cdot {}^3\boldsymbol{\mu}_m)] \cdot \delta\mathbf{r}\}\,dV$$

(41)

Based on the equilibrium Eq. (13), the first term on the right side of Eq. (41) vanishes. Accordingly, relation (40) can be expressed as

$$\frac{1}{V}\int_V [\nabla_m \cdot (\boldsymbol{\sigma}_m - \nabla_m \cdot {}^3\boldsymbol{\mu}_m) \cdot \delta\mathbf{r}]\,dV + \frac{1}{V}\int_V [\nabla_m \cdot ({}^3\boldsymbol{\mu}_m : (\nabla_m \otimes \delta\mathbf{r}))]\,dV = 0.$$

(42)

Using Gauss theorem, Eq. (42) can be transformed into the following form containing the integral over the RVE boundary Γ

$$\frac{1}{V}\int_\Gamma [\mathbf{n} \cdot (\boldsymbol{\sigma}_m - \nabla_m \cdot {}^3\boldsymbol{\mu}_m) \cdot \delta\mathbf{r}]\,d\Gamma + \frac{1}{V}\int_\Gamma [\mathbf{n} \cdot ({}^3\boldsymbol{\mu}_m : (\nabla_m \otimes \delta\mathbf{r}))]\,d\Gamma = 0.$$

(43)

In case of the gradient generalized periodic b. c., the microfluctuations do not contribute to the work performed on the RVE due to the periodicity assumption and the suppression of the corner microfluctuations. The microfluctuations on the RVE boundaries are also suppressed

in case of the gradient displacement b. c., which means that both terms in the Eq. (43) vanish. Since the microfluctuation terms disappear from (37), it is easy to conclude that the homogenized stresses are

$$\boldsymbol{\sigma}_M = \frac{1}{V}\int_V \boldsymbol{\sigma}_m\,dV,$$

(44)

$${}^3\boldsymbol{\mu}_M = \frac{1}{V}\int_V ({}^3\boldsymbol{\mu}_m + \boldsymbol{\sigma}_m \otimes \mathbf{x})\,dV.$$

(45)

In Eq. (45) there is a clear distinction in the definition of the homogenized second-order stress in comparison to the NL-SL homogenization approach. The first term in the bracket represents an intrinsic second-order stress at the microlevel, and the second one is the Cauchy stress multiplied by the position vector, which is used in the NL-SL homogenization. In the NL-NL homogenization the second term basically represents the contribution of the inhomogeneous Cauchy stress distribution to the homogenized higher-order stress. For homogeneous stress states, this term vanishes.

After homogenization of the stress variables, the macroscopic constitutive tangents should be derived. At the microlevel, the material behavior of every constituent can be described by one constitutive operator. But, for the consideration of a heterogeneous microstructure, one constitutive operator at the macroscale cannot capture all the microstructural effects which occur on the RVE. Therefore, the generalized Aifantis macroscopic constitutive relations are assumed, where the updates of the macrolevel stresses are performed by the following incremental relation

$$\Delta\boldsymbol{\sigma}_M = {}^4\mathbf{C}_{\sigma\varepsilon} : \Delta\boldsymbol{\varepsilon}_M + {}^5\mathbf{C}_{\sigma\varepsilon_{x_1}} : \Delta({}^3\boldsymbol{\varepsilon}_{x_1})_M + {}^5\mathbf{C}_{\sigma\varepsilon_{x_2}} : \Delta({}^3\boldsymbol{\varepsilon}_{x_2})_M,$$

(46)

$$\Delta\left({}^3\boldsymbol{\mu}_{x_1}\right)_M = {}^5\mathbf{C}_{\mu_{x_1}\varepsilon} : \Delta\boldsymbol{\varepsilon}_M + {}^6\mathbf{C}_{\mu_{x_1}\varepsilon_{x_1}} : \Delta({}^3\boldsymbol{\varepsilon}_{x_1})_M + {}^6\mathbf{C}_{\mu_{x_1}\varepsilon_{x_2}} : \Delta({}^3\boldsymbol{\varepsilon}_{x_2})_M,$$

(47)

$$\Delta\left({}^3\boldsymbol{\mu}_{x_2}\right)_M = {}^5\mathbf{C}_{\mu_{x_2}\varepsilon} : \Delta\boldsymbol{\varepsilon}_M + {}^6\mathbf{C}_{\mu_{x_2}\varepsilon_{x_1}} : \Delta({}^3\boldsymbol{\varepsilon}_{x_1})_M + {}^6\mathbf{C}_{\mu_{x_2}\varepsilon_{x_2}} : \Delta({}^3\boldsymbol{\varepsilon}_{x_2})_M.$$

(48)

Using the static condensation procedure, already explained in [14,16], leads to nine constitutive operators which may be written as

$$\mathbf{C}_{\sigma\varepsilon} = \frac{1}{V}\mathbf{D}\widetilde{\mathbf{K}}_{bb}\mathbf{D}^T, \qquad \mathbf{C}_{\sigma\varepsilon_{x_1}} = \frac{1}{V}\mathbf{D}\widetilde{\mathbf{K}}_{bb}\mathbf{H}_1^T, \qquad \mathbf{C}_{\sigma\varepsilon_{x_2}} = \frac{1}{V}\mathbf{D}\widetilde{\mathbf{K}}_{bb}\mathbf{H}_2^T,$$
$$\mathbf{C}_{\mu_{x_1}\varepsilon} = \frac{1}{V}\mathbf{H}_1\widetilde{\mathbf{K}}_{bb}\mathbf{D}^T, \quad \mathbf{C}_{\mu_{x_1}\varepsilon_{x_1}} = \frac{1}{V}\mathbf{H}_1\widetilde{\mathbf{K}}_{bb}\mathbf{H}_1^T, \quad \mathbf{C}_{\mu_{x_1}\varepsilon_{x_2}} = \frac{1}{V}\mathbf{H}_1\widetilde{\mathbf{K}}_{bb}\mathbf{H}_2^T,$$
$$\mathbf{C}_{\mu_{x_2}\varepsilon} = \frac{1}{V}\mathbf{H}_2\widetilde{\mathbf{K}}_{bb}\mathbf{D}^T, \quad \mathbf{C}_{\mu_{x_2}\varepsilon_{x_1}} = \frac{1}{V}\mathbf{H}_2\widetilde{\mathbf{K}}_{bb}\mathbf{H}_1^T, \quad \mathbf{C}_{\mu_{x_2}\varepsilon_{x_2}} = \frac{1}{V}\mathbf{H}_2\widetilde{\mathbf{K}}_{bb}\mathbf{H}_2^T.$$

(49)

As usual in homogenization, the constitutive operators are dependent on the condensed RVE stiffness matrix $\widetilde{\mathbf{K}}_{bb}$. It can be observed that the Aifantis microstructural parameter is omitted in the macrolevel constitutive relations because the microstructural parameter cannot be used explicitly on both scales. Basically, the microstructural parameter is defined on the RVE, and it participates in an assembly of the RVE global stiffness matrix. After the homogenization, the contribution of the microstructural parameter is observable through the constitutive operators. More details on the NL-NL homogenization can be found in [49,50].

4.3. Numerical implementation

The derived micro-macro scheme has been implemented into the FE program [46] by means of user subroutines, as shown in Fig. 9. Similar works concerning the implementation of the multiscale framework comprising the first-order homogenization and the NL-SL second-order homogenization into ABAQUS has been carried out in [16,47,51]. Details of the algorithm are displayed in Box 1.

In the NL-NL scheme, both scales are discretized by the C^1 triangular finite element embedded into ABAQUS. Since only the linear elastic behavior is adopted with the Aifantis theory, the homogenization of the constitutive matrices is required only once, for example as the
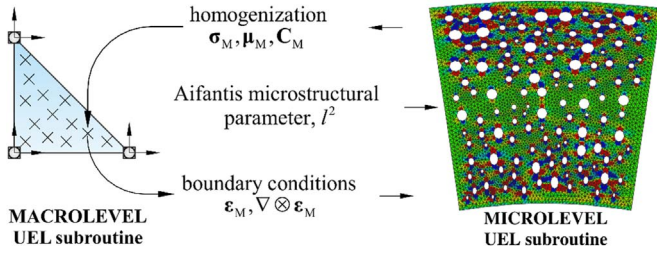
Fig. 9. Scheme of gradient-enhanced second-order homogenization.

preprocessing step. But, in order to observe the phenomena of evolving microstructure, the RVE analysis is necessary, where the stress homogenization is conducted. In the subsequent multiscale procedure two UEL subroutines are running simultaneously. The subroutine of the macrolevel finite element serves as a master routine. It prescribes the RVE boundary conditions based on the macrolevel gradients and runs microlevel analysis as a new ABAQUS boundary value problem. During this period, the master routine is paused awaiting for the input data provided by the homogenization procedure. The RVE boundary value problem is solved by the UEL subroutine of the microscale finite element, where the stress tensors are homogenized and passed to the macrolevel analysis. Therein, the microstructural parameter l^2 must be explicitly defined. Once all necessary data are computed, the macrolevel analysis checks for the convergence and continues.

The presented multiscale scheme has been coded as a „pseudo-parallelized" code, meaning that the computations are performed in an element-by-element manner, where the RVEs for all material points of one macroscale finite element are considered simultaneously.

4.4. Nonlocal behavior in NL-NL homogenization

After establishing the micro-macro framework, the nonlocal effects which occur on the RVE and their influence on the mechanical response of the macrostructure are studied. It is known that the RVE size dictates nonlocality effects through the homogenized double-stress and the constitutive operators in the NL-SL homogenization. On the other hand, in the constitutive model of the NL-NL homogenization the microstructural parameter is present as an intrinsic variable, as well as the RVE size. Generally, both parameters can be changed independently giving nonlocality effects which are expressed by the combination of both parameters. As known, the RVE size L defines some characteristic microstructural size and captures microstructural nonlocal effects. In the authors' approach to the second-order homogenization, besides the RVE size, the Aifantis microstructural parameter is also available, which appears on the RVE. Hence, the RVE represents the microstruc-

ture and the Aifantis parameter represents some characteristic material length scale beneath microstructural level. This means that the authors' contribution could be considered as a "three-scale" scheme. Thus, the relation between nonlocal influence of the RVE size and the parameter l should be identified. Consequently, the nonlocal influence of the two parameters will be described by one "effective" parameter, l_{eff}. In the NL-SL homogenization there is a known nonlocality correlation between the Aifantis theory and the Mindlin's gradient continuum theory identified by the relation between the Aifantis microstructural parameter l and the RVE size L, derived in [5,52] as

$$l^2 = \frac{L^2}{12}. \tag{50}$$

Unfortunately, relation (50) gives correlation among two approaches, but it does not resolve the issue when both parameters are present in a single numerical model. However, in the following example it will be shown that the correlation also exist in case of both parameters. It is easy to prove that the following relation exists between l and L

$$l_{\text{eff}}^2 = l^2 + \frac{L^2}{12}. \tag{51}$$

On the other words, a new "effective" microstructural parameter is expressed, which may be considered as an intrinsic variable in the NL-NL homogenization emerging from the RVE size as well the material related Aifantis microstructural parameter. By virtue of Eq. (51) those two parameters are unified into one "effective" material length scale parameter, which takes into account the contribution of the microstructure and captures mechanisms which take place below the microstructural size.

5. Numerical examples

5.1. Shear layer problem

As an example, the shear layer problem has been analyzed which is usually used as a benchmark test in multiscale homogenization approaches. This benchmark problem has already been considered in the authors' previous publications [16,47], too. In this paper, the previous results for a small strain framework obtained by the NL-SL homogenization are compared to the NL-NL scheme here proposed. To make results obtained by the two distinct approaches comparable, Eq. (51) is used as a link. The same RVE sizes in two homogenization approaches should exhibit an equivalent behavior for the microstructural parameter $l^2 = 0$. The macromodel of the heterogeneous strip with prescribed boundary conditions is presented in Fig. 10. The strip of the

Box 1. Scheme of the NL-NL micro-macro algorithm.

PREPROCESSING STEP
Homogenization of the macroscopic constitutive behavior, Eq. (46)

↓

MULTISCALE ANALYSIS

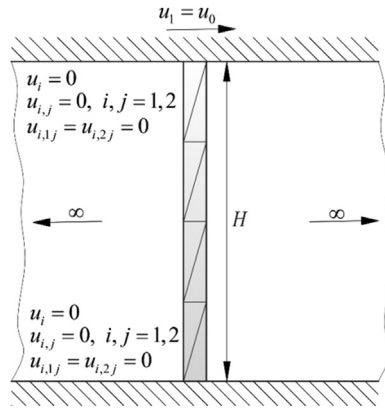| **Macrolevel**		**Microlevel**
1. Start analysis		
2. Apply new increment of the load		
3. New iteration		
Compute ε_M, $\nabla \otimes \varepsilon_M$	ε_M, $\nabla \otimes \varepsilon_M$ →	Prescribe boundary conditions, Eq. (34)
		Solve RVE boundary value problem
4. Store homogenized results	← σ_M, $^3\mu_M$	Compute σ_M, $^3\mu_M$, Eqs. (41) and (42)
5. Check for convergence:		
If converged → step 2		
Else → step 3		

Fig. 10. Shear strip.

height of $H = 10$ mm is clamped at the top and bottom edges and it has an infinite length in the horizontal direction. The horizontal displacement of $u_0 = 0.005$ mm is imposed at the upper edge.

An academic example of a porous steel with 13% of porosity has been used, presented by the RVE of side length $L = 0.2$ mm. The material properties of the matrix material are Young's modulus $E = 210$ GPa and Poisson's ratio $\nu = 0.3$. The discretizations of the RVE used in both the NL-SL and the NL-NL homogenization are shown in Fig. 11. The RVE in the NL-SL homogenization is discretized by 508 CPE4 ABAQUS finite elements, while discretization of the RVE in the NL-NL approach consists of 486 C1PE3 elements. The convergence of the homogenized results in the NL-NL homogenization has been tested in [42]. It has been concluded that the mesh density of the RVE which gives the convergence of the homogenized results is much coarser than the mesh density required for an appropriate description of the RVE geometry. Accordingly, for the chosen RVE, the results obtained by the NL-NL homogenization can be achieved even by a coarser mesh. However, the authors find that the discretization of the RVE represented in Fig. 11b is a lower limit to adequately capture the circular geometry of the holes.

In the NL-NL homogenization the gradient displacement and the gradient generalized periodic boundary conditions have been used. To verify the newly developed multiscale scheme, the results of the NL-NL homogenization have been compared to the NL-SL homogenization comprising the generalized periodic boundary conditions. The distribution of the first and the second displacement derivatives through the height of the strip is presented in Figs. 12 and 13. As can be seen, both homogenization approaches show identical results, proving the identities derived in the paper.

From Figs. 12 and 13 it is obvious that Eq. (51) is valid for $l^2 = 0$. Next, it is necessary to demonstrate that (51) also holds for $l^2 \neq 0$. For this purpose, the two more RVEs of larger size, representing the same heterogeneous material have been introduced. First, the larger RVE is
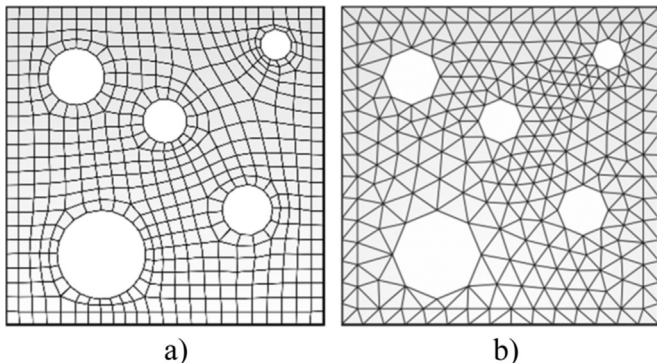

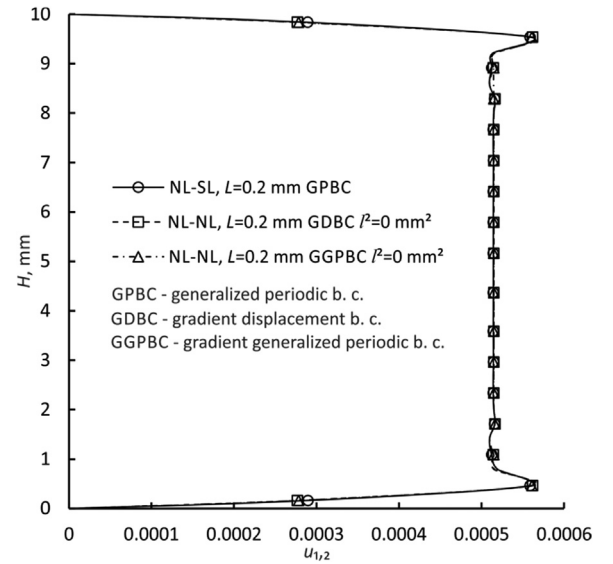**Fig. 11.** RVE of side length $L = 0.2$ mm discretized by: a) 508 CPE4 elements, b) 486 C1PE3 elements.

Fig. 12. Distribution of displacement gradient $u_{1,2}$ for RVE side length 0.2 mm.
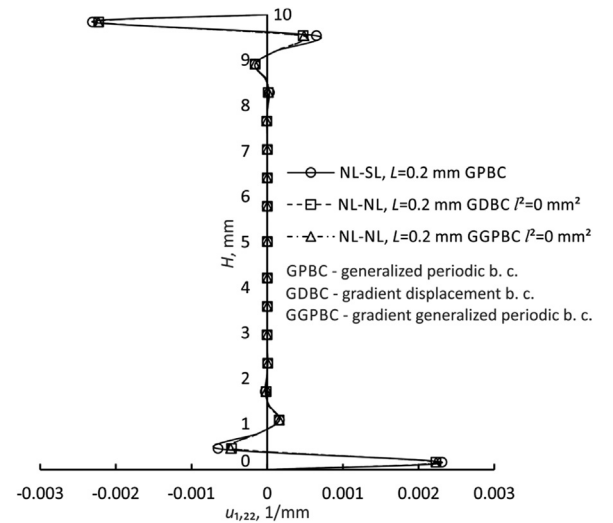

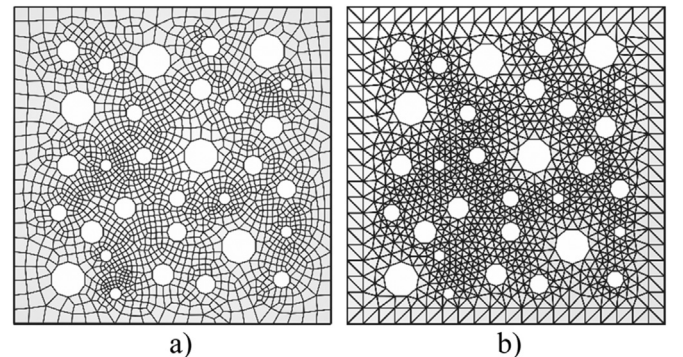**Fig. 13.** Distribution of second-order displacement gradient $u_{1,22}$ for RVE side length 0.2 mm.

Fig. 14. RVE of side length $L = 0.5$ mm discretized by: a) 1779 CPE4 elements, b) 2205 C1PE3 elements.

presented in Fig. 14, where the RVE of side length 0.5 mm is shown, discretized by the CPE4 and the C1PE3 elements. The second larger RVE of side length 1 mm is presented in Fig. 15.

In the following figures the distribution of the first and the second-order displacement derivatives for the two homogenization approaches
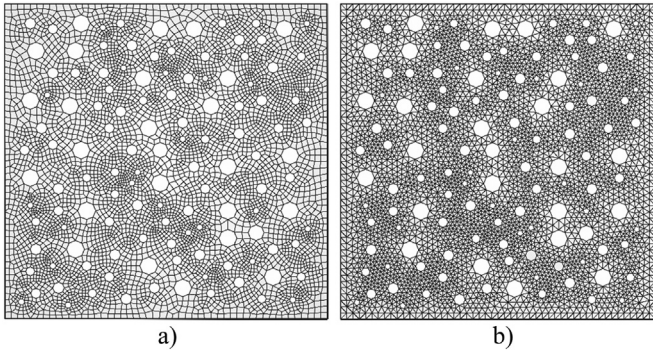
Fig. 15. RVE of side length $L = 1$ mm discretized by: a) 5567 CPE4 elements, b) 8380 C1PE3 elements.
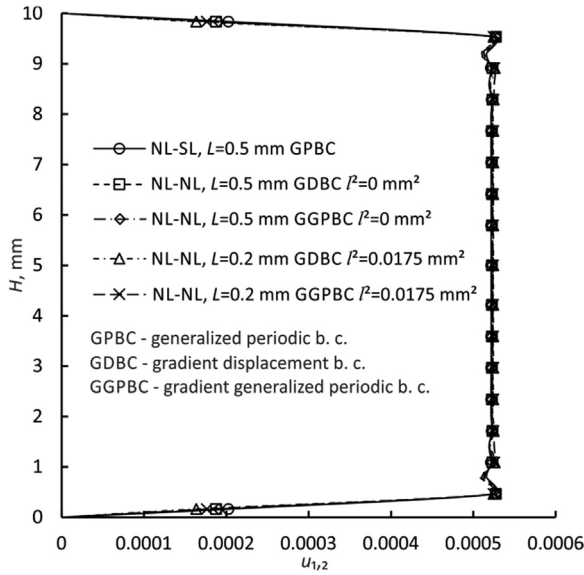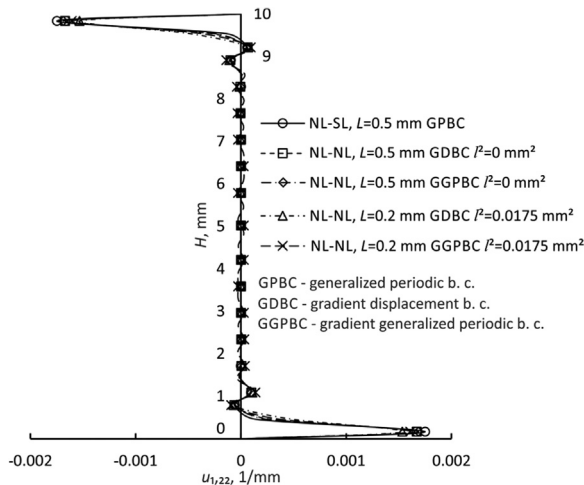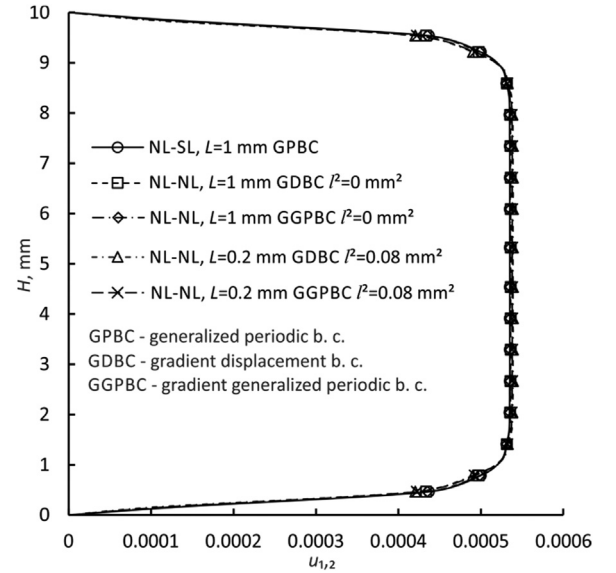

Fig. 16. Distribution of displacement gradient $u_{1,2}$ for RVE side length 0.5 mm.

is presented for the RVE sizes 0.5 and 1 mm and compared with the values associated to the RVE of 0.2 mm.

The distributions presented in Figs. 16–19 demonstrate the formulation validity in the NL-NL homogenization. As the first, all distributions of gradients for the RVE sizes of 0.5 and 1 mm used in both the NL-SL and the NL-NL homogenization schemes are identical. As the second,

Fig. 17. Distribution of second-order displacement gradient $u_{1,22}$ for RVE side length 0.5 mm.

Fig. 18. Distribution of displacement gradient $u_{1,2}$ for RVE side length 1 mm.
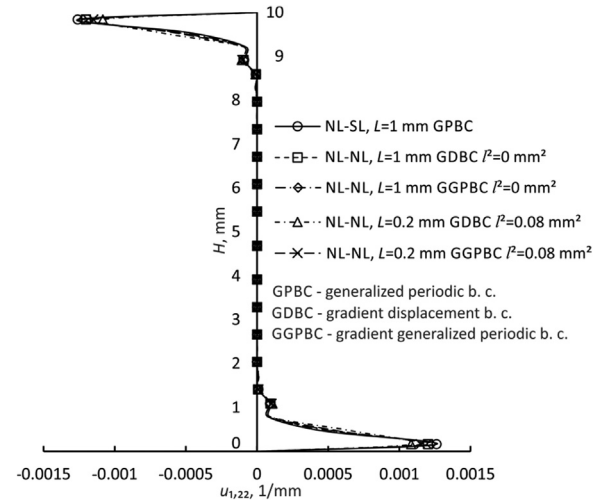

Fig. 19. Distribution of second-order displacement gradient $u_{1,22}$ for RVE side length 1 mm.

the ability of the NL-NL approach to encompass nonlocal effects by a combination of the RVE size and the microstructural parameter l has been demonstrated. In Figs. 16 and 17, there are results for the RVE of side length 0.2 mm used in the NL-NL homogenization. To recover the RVE size difference to 0.5 mm on the basis of Eq. (51), an appropriate measure of $l^2 = 0.0175$ mm² is calculated and prescribed to the material model of the matrix material. In the same way, in Figs. 18 and 19, besides the RVE with side length of 1 mm, the five times smaller RVE has been used in the NL-NL homogenization, and the microstructural parameter of $l^2 = 0.08$ mm² has been added into the material model to encompass equivalent nonlocal behavior. The equivalent distributions of gradients are achieved using the gradient displacement and the gradient generalized periodic boundary conditions.

For the same RVE size, presented in Figs. 14 and 15, in the NL-SL and the NL-NL framework, it is clear that the smaller number of integration points and degrees of freedom in the quadrilateral finite element exhibit better computational efficiency in comparison to the C1PE3 formulation. However, by virtue of the nonlocal theory adopted on the RVE, a single RVE size (Fig. 11b) in the NL-NL homogenization can encompass unlimited range of nonlocal behavior mechanisms, using the Aifantis intrinsic microstructural parameter. Basically, the nonlocal effects described by the RVEs in Figs. 14b and 15b can also be
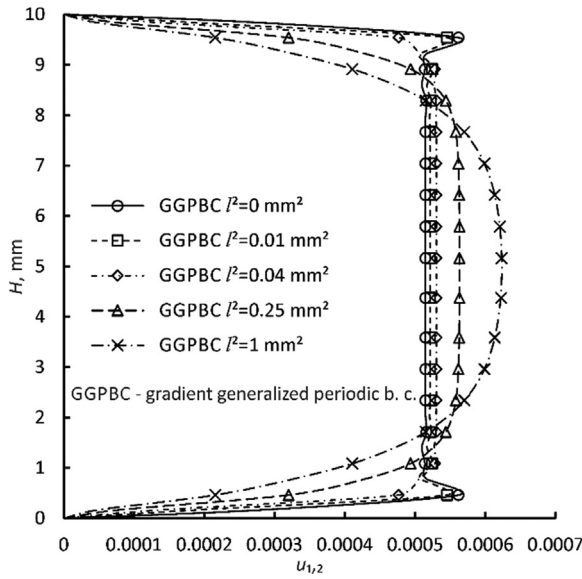
Fig. 20. Distribution of displacement gradient $u_{1,2}$ for RVE side length 0.2 mm and various microstructural parameter values.

Fig. 22. Distribution of displacement gradient component $u_{1,2}$ on RVEs through height of the strip.

achieved by the RVE in Fig. 11b and appropriate value of the Aifantis parameter l. On the other hand, in the NL-SL homogenization approach derived in [17,47], one RVE size means only one nonlocal type of behavior described. The capturing of a different nonlocality effects requests for a modeling of a new RVE with different side length and increased number of finite elements (and degrees of freedom). Clearly, such approach is unfavorable, because the increasing of RVE size leads to the numerically inefficient model and longer computation time. However, in [21] a different concept of length scale on the microstructural level has been presented, where the nonlocality is involved through a characteristic size of dominant inelastic microstructural response. In this way, the multiple nonlocal responses embedded through elastoplastic behavior can be captured on one RVE size.

Hence, it can be concluded that the NL-NL homogenization offers a great numerical advantage. After the successful verification of the NL-NL scheme, a series of analyses of the shear layer problem have been conducted, using various values of l^2 and the constant RVE size of $L = 0.2$ mm. Based on relation (51), the value of l_{eff} is changing, and various types of the shear layer deformation responses are exhibited as displayed in Figs. 20 and 21.
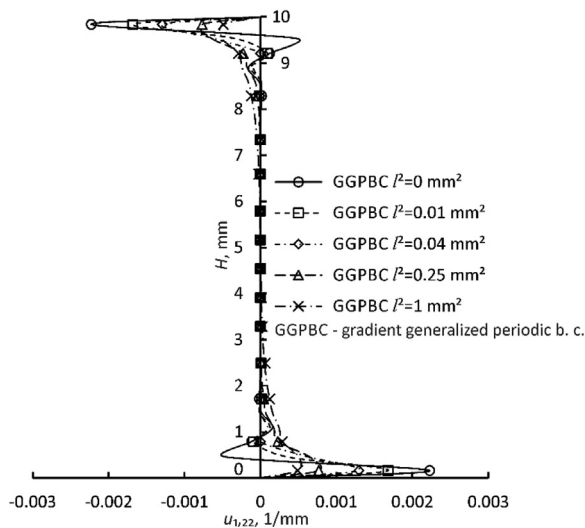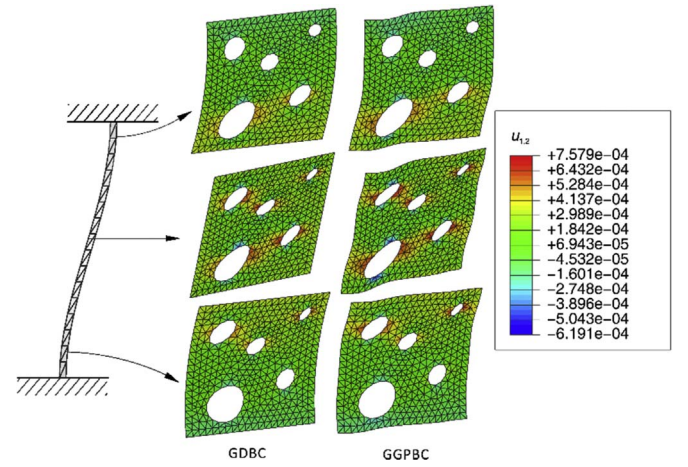
Herein the two characteristic zones can be distinguished. The first zone is near the lower and upper clamp, where high gradients occur. Away from the clamps, in the middle of the strip a pure shear mode is dominant. As can be seen, with the increase of l^2, the width of the middle shear zone is reduced, while the width of the transition zone near the clamps rises. For minor values of l^2, there are high gradients appearing near the clamps (see Fig. 21). With the increase of l^2, which causes stiffer material behavior, these high gradient peaks exceed into smooth change. The distribution of displacement gradient component $u_{1,2}$ for some characteristic RVEs through the height of the strip for $L = 0.2$ mm and $l^2 = 0$ is visualized in Fig. 22. Here the RVE deformation responses under the gradient displacement and the gradient generalized periodic b. c. are compared. It can be seen that the gradient displacement boundary conditions provide stiffer behavior due to the suppression of microfluctuations. It is to note that the deformed RVE shapes presented correspond to the authors' previous results in the NL-SL homogenization [16]. Furthermore, the distribution of the second-order displacement gradient $u_{1,22}$ is displayed in Fig. 23, and it should be stressed that this response is not possible in the case of the NL-SL homogenization approach.

The distinction in the responses associated to the gradient displacement and the periodic b. c. is even more evident in Fig. 23. For both boundary conditions there are high gradients appearing around porosities, physically representing transformation of the circular geometry into the ellipse due to deforming. The changes of curvatures are also present along the RVE edges when the gradient generalized periodic b.
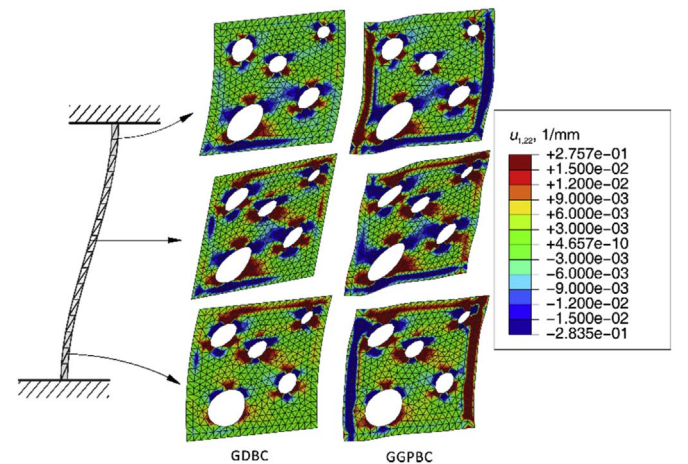

Fig. 21. Distribution of displacement gradient $u_{1,22}$ for RVE side length 0.2 mm and various microstructural parameter values.

Fig. 23. Distribution of second-order displacement gradient component $u_{1,22}$ on RVEs through height of the strip.

c. are imposed, which is not the case for the gradient displacement b. c., which is a clear consequence of the enhanced compliance of the gradient periodic boundary conditions.

6. Conclusions

The paper deals with a new second-order two-scale computational homogenization scheme employing the Aifantis gradient elasticity theory at both macro- and microscale. The basics of the higher-order continuum theory are presented. The proposed formulation of the nonlocal theory is embedded into the finite element framework using of the C^1 three node triangular plane strain finite element.

It has been demonstrated that the employment of nonlocal theory at the microstructural level resolves the inconsistencies arising in the NL-SL homogenization framework available in the literature due to different theories used at various scales. More precisely, the macro-micro correlation of the second-order variables in the NL-NL homogenization scheme is mathematically consistent, since all variables of the macrostructure are also defined on the RVE. Thus, the averaging is possible without any additional integral constraints used for the definition of the higher-order variables on the RVE. On the other hand, the homogenized second-order stress is no more dependent only on the Cauchy stress tensor, as in the NL-SL approach, but it also depends on the second-order stress coming from the microscale. Since the constitutive behavior is generally unknown for a heterogeneous material, the generalized Aifantis constitutive relations are assumed at the macro-level, which leads to the nine constitutive matrices. The gradient displacement and the gradient generalized periodic boundary conditions on the RVE are derived. Another advantage of the NL-NL scheme is observable in the case of boundary conditions. The gradient generalized b. c. are able to prescribe the complete second-order strain tensor from the macrolevel using the derivatives included in the element DOF. In the NL-SL homogenization this is possible only if the microfluctuation integral constraint is prescribed on the RVE boundaries. As known, nonlocality effects in the NL-NL scheme are described by the RVE size and the microstructural parameter. The relation between the internal length scale parameter of the Aifantis theory and the RVE size has been found. Also, a correlation among NL-NL and NL-SL homogenization approach has been derived, expressed by the RVE size. For a specific case when the microstructural parameter $l^2 = 0$, the numerical results obtained by the NL-NL approach are comparable to the results gained by the NL-SL scheme, because the nonlocality of the both approaches is dependent on the RVE size only.

All algorithms developed are embedded into the FE software ABAQUS. The verification of the proposed numerical procedure has been performed using a standard benchmark problem of heterogeneous strip loaded to shear by a horizontal displacement. To demonstrate accuracy of the formulation presented, the results obtained by the NL-NL homogenization scheme are compared to the NL-SL approach for $l^2 = 0$. The advantage of the NL-NL homogenization has been demonstrated in the description of size effects, where the RVE size has been kept constant, while the microstructural parameter has been increased.

The employment of the nonlocal continuum theory at the microscale has shown the better efficiency in comparison to the available NL-SL homogenization scheme. Furthermore, the application of the nonlocal theory on the RVE offers several advantages, such as advanced nonlocality description, or a firm ground for the future research directions in the field of multiscale modeling of damage phenomena.

References

[1] Čanžar P, Tonković Z, Kodvanj J. Microstructure influence on fatigue behaviour of nodular cast iron. Mater Sci Eng: A 2012;556:88–99.

[2] Hassani B, Hinton E. A review of homogenization and topology opimization II - analytical and numerical solution of homogenization equations. Comput Struct 1998;69:719–38.

[3] Doghri I, Ouaar A. Homogenization of two-phase elasto-plastic composite materials and structures: study of tangent operators, cyclic plasticity and numerical algorithms. Int J Solids Struct 2003;40:1681–712.

[4] Arabnejad S, Pasini D. Mechanical properties of lattice materials via asymptotic homogenization and comparison with alternative homogenization methods. Int J Mech Sci 2013;77:249–62.

[5] Kouznetsova VG, Geers M, Brekelmans WAM. Size of a representative volume element in a second-order computational homogenization framework. Int J Multiscale Comput Eng 2004;2:24.

[6] Kaczmarczyk LK, Pearce CJ, Bicanic N. Scale transition and enforcement of RVE boundary conditions in second-order computational homogenization. Int J Numer Methods Eng 2008;74:506–22.

[7] Aliabadi MHF, Ugo G. Multiscale Modeling in Solid Mechanics. London: Imperial College Press; 2010.

[8] Temizer Ä, Wriggers P. An adaptive multiscale resolution strategy for the finite deformation analysis of microheterogeneous structures. Comput Methods Appl Mech Eng 2011;200:2639–61.

[9] Wu T, Temizer İ, Wriggers P. Computational thermal homogenization of concrete. Cem Concr Compos 2013;35:59–70.

[10] Niekamp R, Markovic D, Ibrahimbegovic A, Matthies HG, Taylor RL. Multi-scale modelling of heterogeneous structures with inelastic constitutive behavior. Eng Comput 2009;26:6–28.

[11] Gruttmann F, Wagner W. A coupled two-scale shell model with applications to layered structures. Int J Numer Methods Eng 2013;94:1233–54.

[12] Matsuda T, Ito T, Akimoto S, Kobori H, Goto K, Takano N. Macro/micro simultaneous validation for multiscale analysis of semi-periodically perforated plate using full-field strain measurement. Int J Mech Sci 2016;110:34–40.

[13] Miehe C, Koch A. Computational micro-to-macro transitions of discretized microstructures undergoing small strains. Arch Appl Mech 2002;72:300–17.

[14] Kouznetsova V, Brekelmans WAM, Baaijens FPT. An approach to micro-macro modeling of heterogeneous materials. Comput Mech 2001;27:37–48.

[15] Feyel F, Chaboche JL. FE2 multiscale approach for modelling the elastoviscoplastic behaviour of long fibre SiC/Ti composite materials. Comput Methods Appl Mech Eng 2000;183:309–30.

[16] Lesičar T, Tonković Z, Sorić J. A second-order two-scale homogenization procedure using C1 macrolevel discretization. Comput Mech 2014;54:425–41.

[17] Kouznetsova VG, Geers MGD, Brekelmans WAM. Multi-scale second-order computational homogenization of multi-phase materials: a nested finite element solution strategy. Comput Methods Appl Mech Eng 2004;193:5525–50.

[18] Mindlin RD. Second gradient of strain and surface-tension in linear elasticity. Int J Solids Struct 1965;1:417–38.

[19] Toupin RA. Elastic materials with couple-stresses. Arch Ration Mech Anal 1962;11:385–414.

[20] Kouznetsova V, Geers MGD, Brekelmans WAM. Multi-scale constitutive modelling of heterogeneous materials with a gradient-enhanced computational homogenization scheme. Int J Numer Methods Eng 2002;54:1235–60.

[21] Luscher DJ, McDowell DL, Bronkhorst CA. A second gradient theoretical framework for hierarchical multiscale modeling of materials. Int J Plast 2010;26:1248–75.

[22] D. Luscher, D. McDowell, C. Bronkhorst, Essential Features Of Fine Scale Boundary Conditions For Second Gradient Multiscale Homogenization Of Statistical Volume Elements, 10, 2012, 461–486.

[23] Blanco PJ, Sánchez PJ, de Souza EA, Neto, Feijóo RA. The method of multiscale virtual power for the derivation of a second order mechanical model. Mech Mater 2016;99:53–67.

[24] Xia ZC, Hutchinson JW. Crack tip fields in strain gradient plasticity. J Mech Phys Solids 1996;44:1621–48.

[25] Shu JY, Fleck NA. The prediction of a size effect in microindentation. Int J Solids Struct 1998;35:1363–83.

[26] Amanatidou E, Aravas N. Mixed finite element formulations of strain-gradient elasticity problems. Comput Methods Appl Mech Eng 2002;191:1723–51.

[27] Shu JY, King WE, Fleck NA. Finite elements for materials with strain gradient effects. Int J Numer Methods Eng 1999;44:373–91.

[28] Matsushima T, Chambon R, Caillerie D. Large strain finite element analysis of a local second gradient model: application to localization. Int J Numer Methods Eng 2002;54:499–521.

[29] Zervos A, Papanicolopulos S, Vardoulakis I. Two finite-element discretizations for gradient elasticity. J Eng Mech 2009;135:203–13.

[30] Papanicolopulos SA, Zervos A, Vardoulakis I. A three-dimensional C1 finite element for gradient elasticity. Int J Numer Methods Eng 2009;77:1396–415.

[31] Borst Rd, Pamin J. A gradient plasticity approach to finite element predictions of soil instability. Arch Mech 1995;47:353–77.

[32] Engel G, Garikipati K, Hughes TJR, Larson MG, Mazzei L, Taylor RL. Continuous/discontinuous finite element approximations of fourth-order elliptic problems in structural and continuum mechanics with applications to thin beams and plates, and strain gradient elasticity. Comput Methods Appl Mech Eng 2002;191:3669–750.

[33] Chandran RB. Development of discontinuous Galerkin method for nonlocal linear elasticity, Ph.D. Massachusetts Institute of Technology; 2007.

[34] Askes H, Aifantis EC. Gradient elasticity in statics and dynamics: an overview of formulations, length scale identification procedures, finite element implementations and new results. Int J Solids Struct 2011;48:1962–90.

[35] Tang Z, Shen S, Atluri SN. Analysis of materials with strain-gradient effects: a meshless local Petrov-Galerkin (MLPG) approach, with nodal displacements only. CMES - Comput Model Eng Sci 2003;4:177–96.

[36] Skatulla S, Arockiarajan A, Sansour C. A nonlinear generalized continuum approach for electro-elasticity including scale effects. J Mech Phys Solids 2009;57:137–60.

[37] Polyzos D, Tsepoura KG, Tsinopoulos SV, Beskos DE. A boundary element method for solving 2-dand 3-D static gradient elastic problems: Part I: integral formulation. Comput Methods Appl Mech Eng 2003;192:2845–73.

[38] Karlis GF, Tsinopoulos SV, Polyzos D, Beskos DE. Boundary element analysis of mode I and mixed mode (I and II) crack problems of 2-D gradient elasticity. Comput Methods Appl Mech Eng 2007;196:5092–103.

[39] Papacharalampopoulos A, Karlis GF, Charalambopoulos A, Polyzos D. BEM solutions for 2D and 3D Dynamic problems in Mindlin's strain gradient theory of elasticity. CMES: Comput Model Eng Sci 2010;58:45–75.

[40] Dong L, Alotaibi A, Mohiuddine SA, Atluri SN. Computational methods in engineering: a variety of Primal & mixed methods, with Global & local Interpolations, for well-posed or ill-posed BCs. CMES - Comput Model Eng Sci 2014;99:1–85.

[41] Lesičar T, Tonković Z, Sorić J. C1 continuity finite element formulation in second-order computational homogenization scheme. J Multiscale Model 2012;04:1250013.

[42] Lesičar T, Tonković Z, Sorić J. Second-order computational homogenization scheme preserving microlevel C1 continuity. Key Eng Mater 2015;627:381–4.

[43] Mindlin RD, Eshel NN. On first strain-gradient theories in linear elasticity. Int J Solids Struct 1968;4:109–24.

[44] Altan SB, Aifantis EC. On the structure of the mode III crack-tip in gradient elasticity. Scr Metall Et Mater 1992;26:319–24.

[45] Lesičar T, Tonković Z, Sorić J. Boundary conditions in a multiscale homogenization procedure. Key Eng Mater 2013;577–578:297–300.

[46] ABAQUS. ABAQUS/Standard, in: ABAQUS, Dassault Systemes, Providence, RI, USA; 2014.

[47] Lesičar T, Sorić J, Tonković Z. Large strain, two-scale computational approach using continuity finite element employing a second gradient theory. Comput Methods Appl Mech Eng 2016;298:303–24.

[48] Nguyen VD, Becker G, Noels L. Multiscale computational homogenization methods with a gradient enhanced scheme based on the discontinuous Galerkin formulation. Comput Methods Appl Mech Eng 2013;260:63–77.

[49] Lesičar T. Multiscale modeling of heterogeneous materials using second-order homogenization, Ph.D. Zagreb: University of Zagreb; 2015.

[50] Lesičar T, Tonković Z, Sorić J. Second-order computational homogenization approach using higher-order gradients at microlevel. Key Eng Mater 2016;665:181–4.

[51] Yuan Z, Fish J. Toward realization of computational homogenization in practice. Int J Numer Methods Eng 2008;73:361–80.

[52] Gitman IM, Askes H, Aifantis EC. The representative volume size in static and dynamic micro-macro transitions. Int J Fract 2005;135:L3–9.